

JGR Space Physics

RESEARCH ARTICLE

10.1029/2022JA031082

Key Points:

- Broad energy spectra in our observations are due to solar wind protons forming partial ring distributions
- The partial ring distributions form due to solar wind proton trajectories focusing at a density enhancement layer
- From the partial ring distributions we estimate the average upstream magnetic field direction and the average bulk plasma drift velocity

Supporting Information:

Supporting Information may be found in the online version of this article.

Correspondence to:

A. Moeslinger,
anja.moeslinger@irf.se

Citation:

Moeslinger, A., Wieser, G. S., Nilsson, H., Gunell, H., Williamson, H. N., LLera, K., et al. (2023). Solar wind protons forming partial ring distributions at comet 67P. *Journal of Geophysical Research: Space Physics*, 128, e2022JA031082. <https://doi.org/10.1029/2022JA031082>

Received 13 OCT 2022

Accepted 16 JAN 2023

Author Contributions:

Conceptualization: A. Moeslinger, G. Stenberg Wieser, H. Nilsson, H. Gunell

Data curation: A. Moeslinger, G. Stenberg Wieser

Formal analysis: A. Moeslinger, G. Stenberg Wieser

Funding acquisition: H. Nilsson

Investigation: G. Stenberg Wieser, H. Nilsson, K. LLera, E. Odelstad, I. Richter

Methodology: A. Moeslinger, G. Stenberg Wieser, H. Nilsson, H. Gunell

Project Administration: A. Moeslinger, G. Stenberg Wieser, H. Nilsson

Resources: G. Stenberg Wieser, H. Nilsson, K. LLera, E. Odelstad, I. Richter

©2023. The Authors.

This is an open access article under the terms of the [Creative Commons Attribution License](https://creativecommons.org/licenses/by/4.0/), which permits use, distribution and reproduction in any medium, provided the original work is properly cited.

Solar Wind Protons Forming Partial Ring Distributions at Comet 67P

A. Moeslinger^{1,2} , G. Stenberg Wieser¹ , H. Nilsson¹ , H. Gunell² , H. N. Williamson¹ , K. LLera³, E. Odelstad⁴ , and I. Richter⁵ 

¹Swedish Institute of Space Physics, Kiruna, Sweden, ²Department of Physics, Umeå University, Umeå, Sweden, ³Southwest Research Institute, San Antonio, TX, USA, ⁴Swedish Institute of Space Physics, Uppsala, Sweden, ⁵Institut für Geophysik und Extraterrestrische Physik, Technische Universität Braunschweig, Braunschweig, Germany

Abstract We present partial ring distributions of solar wind protons observed by the Rosetta spacecraft at comet 67P/Churyumov-Gerasimenko. The formation of ring distributions is usually associated with high activity comets, where the spatial scales are larger than multiple ion gyroradii. Our observations are made at a low-activity comet at a heliocentric distance of 2.8 AU on 19 April 2016, and the partial rings occur at a spatial scale comparable to the ion gyroradius. We use a new visualization method to simultaneously show the angular distribution of median energy and differential flux. A fitting procedure extracts the bulk speed of the solar wind protons, separated into components parallel and perpendicular to the gyration plane, as well as the gyration velocity. The results are compared with models and put into context of the global comet environment. We find that the formation mechanism of these partial rings of solar wind protons is entirely different from the well-known partial rings of cometary pickup ions at high-activity comets. A density enhancement layer of solar wind protons around the comet is a focal point for proton trajectories originating from different regions of the upstream solar wind. If the spacecraft location coincides with this density enhancement layer, the different trajectories are observed as an energy-angle dispersion and manifest as partial rings in velocity space.

Plain Language Summary Particles of solar origin, called the “solar wind,” flow straight from the Sun in interplanetary space. When this solar wind meets an obstacle, such as a planet, it gets deflected around it. At comet 67P/Churyumov-Gerasimenko, visited by the Rosetta spacecraft from 2014 to 2016, our instrument Rosetta Plasma Consortium (RPC)-Ion Composition Analyzer (ICA) measured the main constituents of this solar wind: protons and alpha particles. When the comet is far away from the Sun, the solar wind protons are usually observed coming from the sunward direction with only slight deflection and constant velocities. On 19 April 2016, the main case for our study, we measure solar wind protons arriving in a wide range of directions. The velocity of these protons depends on how much they have been deflected. This creates partial ring distributions, which we visualize and quantify using a method specifically developed for this purpose. We show that these partial rings are a rare observation of a spatially confined region where solar wind protons from different regions of the solar wind are observed simultaneously.

1. Introduction

Comets are a highly diverse group of solar system bodies that are mainly comprised of ice and organic material (Filacchione et al., 2019). They are known for their vast tails resulting from the ices on their surface sublimating when the comets approach the sun. Cometary activity can be defined by the amount of volatiles that a comet releases into space. An example of a high-activity comet is 1P/Halley, which has been the target of several space missions, for example, ESA’s Giotto mission (Reinhard, 1987). The atmosphere of such high-activity comets, especially at perihelion, can extend millions of kilometres from the nucleus. Low-activity comets (Hansen et al., 2016), such as 67P/Churyumov-Gerasimenko (hereafter 67P), only have a tenuous atmosphere that might span no more than a few thousand kilometres. The cometary activity is driven by the strength of the solar radiation and strongly varies over time due to the comet’s highly elliptical orbit. The significant change in activity also changes the plasma environment around the comet with different plasma boundaries forming at certain heliocentric distances (Mandt et al., 2016).

The Rosetta mission has so far been the only mission to orbit a comet. It accompanied comet 67P for 2 years and observed large variations in its cometary activity as the heliocentric distance changed from about 3.6 AU to 1.24

Software: A. Moeslinger, G. Stenberg Wieser
Supervision: G. Stenberg Wieser, H. Nilsson, H. Gunell
Validation: A. Moeslinger, H. Nilsson, H. N. Williamson, K. LLera, E. Odelstad, I. Richter
Visualization: A. Moeslinger, G. Stenberg Wieser
Writing – original draft: A. Moeslinger, G. Stenberg Wieser, H. Nilsson
Writing – review & editing: A. Moeslinger, G. Stenberg Wieser, H. Nilsson, H. Gunell, H. N. Williamson, K. LLera, E. Odelstad, I. Richter

AU. This provided us with unique measurements of the evolving plasma environment (Glassmeier, Boehnhardt, et al., 2007; Goetz et al., 2022; Taylor et al., 2017). In the beginning of the mission, the low cometary activity presented no significant obstacle to the solar wind, which was observed from the anti-sunward direction with little to no deflection (Behar et al., 2016). At heliocentric distances between approximately 3 AU and 2.2 AU the cometary activity increases, and with it the flux of cometary water-group ions (Nilsson et al., 2017). This also coincides with observations of a more deflected but still beam-like, solar wind (Behar et al., 2017). Closer to perihelion the deflection increases even further, until Rosetta enters a region completely devoid of solar wind protons, the solar wind ion cavity, at around 1.7 AU (Nilsson et al., 2017). During the outbound leg, observations show that the plasma environment evolves in reverse order.

This paper focuses on observations from 19 April 2016, when comet 67P was at 2.8 AU on its outbound journey. Contrary to the expected beam-like and slightly deflected solar wind, observations show partial ring distributions in the proton data. Ring distributions can be formed by two interacting plasma populations. At a comet these are typically the solar wind ions and the cometary ions. When the cometary activity is low the solar wind flow is almost undisturbed and newly born cometary ions are picked up by this flow. The cometary ions, which initially have very low speeds, then form a ring distribution in velocity space if the spatial scales are larger than multiple cometary ion gyroradii (Coates, 2004). As the activity increases and the density of the two particle populations becomes comparable, the situation is more complex. The two populations then gyrate around a common gyrocentre and both form ring distributions in velocity space (Behar et al., 2018).

Ring distributions of cometary ions have been observed at 1P/Halley. Water group ions from the comet were picked up by the solar wind and in the solar wind turbulence pitch angle scattering transformed the initial ring distribution into a shell distribution (Coates et al., 1989). In the case of comet Halley the spatial scale of the coma is large enough to allow for protons released in photo-dissociation of cometary water ions to be picked up and form rings as well. Such proton ring distributions were observed (Neugebauer et al., 1989), but these protons were of cometary origin, and not solar wind protons. At 67P a considerable deflection of the solar wind together with an acceleration of the cometary ions along the solar wind electric field is observed at low to moderate activities (Nilsson et al., 2017). This deflection is the beginning of gyration due to the small spatial scales of the interaction region at comet 67P. Reports on ring distributions are rare, but Williamson et al. (2022) present a case (at higher activity) where both cometary ions and solar wind protons form partial rings in velocity space. These observations have been interpreted as indicative of cometosheath formation. In this region, located downstream of the cometary bow shock, the solar wind slows down and thermalizes, and the plasma density increases.

Numerical models serve to set the local in situ measurements of Rosetta at 67P in a global context and help explain observed phenomena. Hybrid models, for example, presented by Koenders et al. (2015) in the context of 67P, are frequently used to model the interaction between the solar wind and the cometary plasma. There are, of course, limitations. Many models simplify the cometary environment by, for instance, assuming spherically symmetric outgassing. They also require solar wind conditions and cometary activity as input parameters to produce relevant results. Additionally, the spatial resolution of the models is often not high enough to resolve processes occurring close to the nucleus. Nonetheless, hybrid models have been used to aid in understanding unique cometary phenomena, such as the infant bow shock (Gunell et al., 2018). Sometimes very simple models are helpful for interpretation. Behar et al. (2018) developed a 2D semi-analytical model to provide a view on single particle dynamics at the comet. Among other things, it suggests the existence of a solar wind-depleted region, and a local density enhancement of the solar wind along the boundary layer (titled “caustic” in the paper). Although this model does not include electric fields, the particle trajectories resulted in similar features also seen in hybrid models. Such density enhancements have also been reported, e.g., downstream of the Earth’s bow shock (Sckopke et al., 1983). In this paper, we will compare our observational results to models in order to explain the occurrence of partial ring distributions of solar wind protons.

2. Instrument Description

The main data sources for this study are the two ion mass spectrometers on the Rosetta spacecraft: the Ion Composition Analyzer (ICA) and the Ion and Electron Sensor (IES). Both instruments are part of the Rosetta Plasma Consortium (RPC; Carr et al., 2007). IES and ICA are mounted at different locations with different orientations on the spacecraft and provide partially complementary field-of-views, which we will make use of in this

paper. A signal outside of one sensor's field-of-view can therefore be picked up by the other, and the overlapping part of the field-of-view serves as a validation of the observations.

2.1. Ion Composition Analyzer

ICA is a mass-resolving ion spectrometer with a field-of-view of $360^\circ \times 90^\circ$. The field-of-view is subdivided into 16 equally spaced azimuth and elevation bins, giving an angular resolution of 22.5° in azimuth, and approximately 5.6° in elevation (Nilsson et al., 2007). The mass resolution allows to distinguish between H^+ , He^{2+} , He^+ , and heavier ions. The energy range of the instrument is between a few eV and 40 keV, logarithmically distributed over 96 energy bins. Each observation consists of 16 consecutive elevation scans, one for each elevation bin. An elevation scan is made at a set elevation and sweeps over the entire energy range, while azimuth and mass bins are observed continuously. Such a full scan of all variables takes 192 s, which is the nominal time resolution of the instrument. To improve data compression for downlink to Earth, a background count reduction was applied on-board. This removes both noise and very weak signals. The data set used here is mass-separated into H^+ , He^{2+} , and heavy ions, and has been converted to differential flux.

2.2. Ion and Electron Sensor

IES is a combined ion and electron spectrometer, with a field-of-view of $360^\circ \times 90^\circ$ for both sensors. The ion sensor features an angular resolution of $45^\circ \times 5^\circ$, with a high-resolution sector subdivided into $5^\circ \times 5^\circ$ sectors. The angular resolution of electrons is $22.5^\circ \times 5^\circ$ for the entire field-of-view. Both sensors cover the energy range from 1 eV to 22 keV in 124 energy steps and have an energy resolution of 4%. The time resolution can be varied and ranges from 128 to 1024 s.

To comply with telemetry requirements, the data was binned onboard and transmitted with a lower resolution than measured. The available angular resolution of the data used in this study is $45^\circ \times 10^\circ$ for both the ion and the electron sensor. For the energy resolution, two successive measurements were binned together and the time resolution is 256 s (Burch et al., 2007). IES does not apply a background reduction, and the data appear noisier than ICA data. Both ICA and IES have parts of their nominal field-of-view obstructed by the spacecraft. Ions coming from those directions can therefore not be detected by the instrument. An illustration and short description about which pixels are affected can be found in Figure S4 in Supporting Information S1.

2.3. Other Instruments

In addition to data from the ion spectrometers, we use data from the magnetometer (MAG) and the Langmuir probes (LAP), which also are parts of RPC. MAG measures the magnetic field vector with a sampling frequency of 20 Hz. The range is ± 16384 nT with a resolution of 31 pT. Due to instrumental effects, there can be an unknown offset in the measured magnetic field vector on the order of a few nT. If this offset is primarily in the direction perpendicular to the real magnetic field direction, this might result in an unknown bias in the calculated magnetic field direction of up to approximately 15° (Glassmeier, Richter, et al., 2007). The LAP instrument consists of two spherical Langmuir probes placed at the ends of two booms extending 1.6 and 2.2 m from the spacecraft body (Eriksson et al., 2007). From LAP, we retrieve the electron density. More information on the RPC instruments and known data caveats can be found in the RPC User Guide (Beth et al., 2019). Finally, we estimate the neutral gas cometary production rate using data from the COmet Pressure Sensor (COPS, part of the ROSINA package; Balsiger et al., 2007). COPS consists of two pressure gauges giving the neutral density and dynamic pressure of the gas streaming out from the comet. The measured neutral density is converted to a comet production rate assuming spherically symmetric outgassing (Haser, 1957).

3. Methods

3.1. Dual Colormap Plots

Commonly used heatmaps allow for a graphical representation of only one variable (e.g., flux). An example is the energy-time spectrogram (top panel in Figure 2) displaying the differential flux of ions as a function of energy and time, summed over the entire field-of-view. Similarly, one can make a heatmap of the differential flux as a

function of the field-of-view, summed over all energies and for a certain time interval. To simultaneously study dependence on both energy and flow direction of the ions, we use a dual colormap showing both the differential flux and the median energy of the ions as a function of the instruments' field-of-view at the highest possible time resolution (see e.g., Figure 3).

To combine two quantities into one dual colormap with intuitive identification of both individual variables, we use the CIECAM02 color appearance model (Moroney et al., 2002). CIECAM02 computes so-called perceptual attribute correlates from perceived colors and is based on experimental data (Luo & Hunt, 1998). For simplicity, we will refer to the perceptual attributes as hue, brightness, and chroma (often also called saturation). These independent variables create a three-dimensional color space. The dual colormap plots are a two-dimensional slice of this color space at a fixed chroma value. Our two variables of interest, the median energy and the differential flux, are mapped onto the two axes of this color slice: different values of the median energy are represented by a different hue, while the differential flux determines the brightness of each data point. An example of how the different parameters affect the result is illustrated in Figure S3 in Supporting Information S1. The obtained color in CIECAM02 variable space is then converted to an RGB triple using `colspace`, cropping any values that fall outside of minimum/maximum boundaries. A similar approach to fuse two images containing complementary data has been used in medical science (Li et al., 2014).

3.2. Partial Ring Fits

To characterize the observed partial rings, we fit a circle to the data in velocity space. For each scan covering the full field-of view (corresponding to 192 s for ICA and 256 s for IES), we convert the median energy of each azimuth-elevation pixel into a velocity vector with an associated differential flux. The median energy is calculated as a weighted median using the differential flux of each individual energy bin. It is defined as the energy bin where the differential flux integrated up to this energy exceeds half of the total flux. Depending on the precise time, there are usually 15 to 25 velocity vectors with a differential flux larger than a threshold value (nonzero for ICA, and 1.5 orders of magnitude lower than the maximum value for IES due to the higher noise level of IES). The circle is found through a non-linear least square fitting process that is divided into two steps:

1. Fit a plane to all datapoints
2. Fit a sphere to the datapoints, where the center of the sphere must lie on the plane determined in step 1

The two-step process improves the robustness of the fitting procedure compared to a one-step fitting procedure and restricts the number of free variables to match the degrees of freedom in the system.

In the first step, we retrieve $\mathbf{u}_{\text{bulk},\parallel}$, a vector normal to the plane best describing the location of the velocity vectors. In an ideal case with a uniform magnetic field $\mathbf{u}_{\text{bulk},\parallel}$ would be along the ambient magnetic field. We find $\mathbf{u}_{\text{bulk},\parallel}$ by minimizing

$$f_1(\mathbf{u}_i) = \sum_{\mathbf{u}_i} w(\mathbf{u}_i) (\hat{\mathbf{u}}_{\text{bulk},\parallel} \cdot (\mathbf{u}_i - \mathbf{u}_{\text{bulk},\parallel})), \quad (1)$$

where \mathbf{u}_i are the velocity vectors with differential fluxes above the threshold value and $\hat{\mathbf{u}}_{\text{bulk},\parallel}$ is the unit vector along $\mathbf{u}_{\text{bulk},\parallel}$. The weighting function $w(\mathbf{u}_i)$ is the logarithm of the differential flux associated with the vector \mathbf{u}_i .

In the second step, we find the center \mathbf{u}_0 and radius u_{\perp} of the sphere that best represents the velocity vectors. We require the center of the sphere to lie on the plane determined in the first step. The fitting parameters are obtained by minimizing

$$f_2(\mathbf{u}_i) = \sum_{\mathbf{u}_i} w(\mathbf{u}_i) (|\mathbf{u}_0 - \mathbf{u}_i|^2 - u_{\perp}^2), \quad (2)$$

where we use the same weighting as in step 1. The fit parameter u_{\perp} corresponds to a gyration speed, and the difference between the center of the sphere and $\mathbf{u}_{\text{bulk},\parallel}$ is the drift velocity in the plane of the velocity vectors, $\mathbf{u}_{\text{drift}} = \mathbf{u}_0 - \mathbf{u}_{\text{bulk},\parallel}$, see Figure 1. This additional drift motion, e.g., due to an $\mathbf{E} \times \mathbf{B}$ drift, is the cause of $\mathbf{u}_{\text{bulk},\parallel}$ being different from the center of gyration \mathbf{u}_0 .

3.2.1. Partial Ring Extent

We define the extent of the partial ring as the angle corresponding to the arc along the fitted ring spanned by the observed data points with fluxes above the threshold value (see Figure 1). A complete ring would correspond

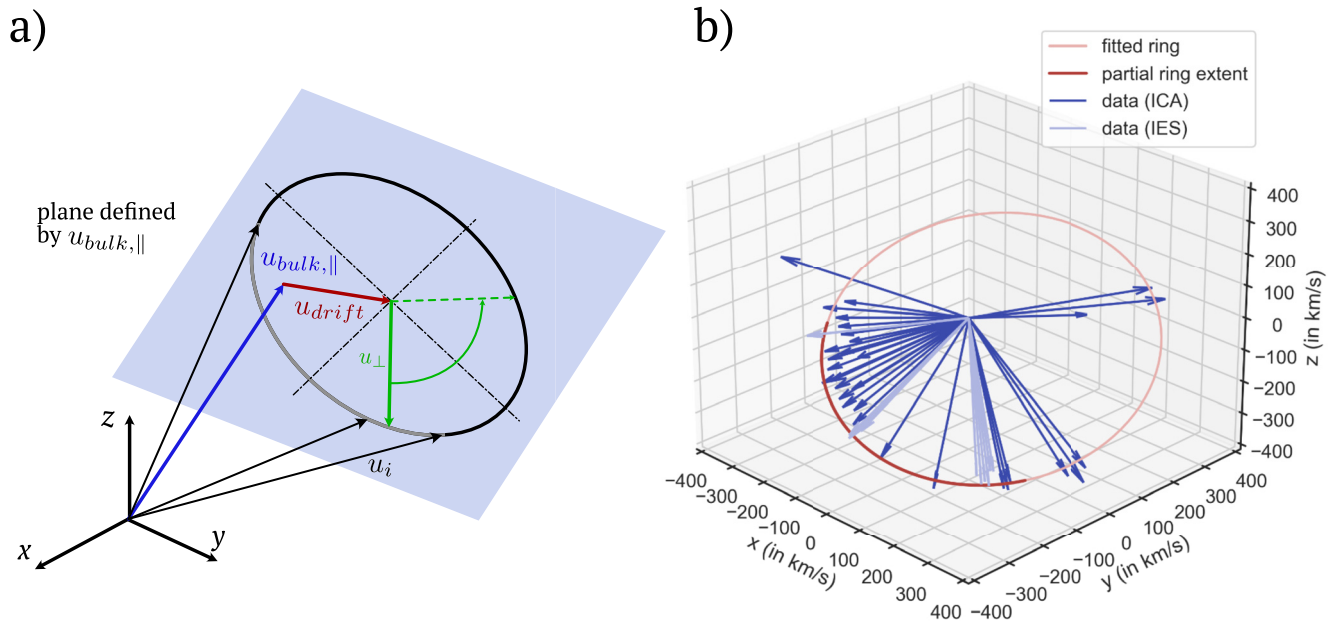


Figure 1. (Partial) Rings in velocity space. Panel (a): Illustration of a generic ring in 3D velocity space, with the defining parameters $\mathbf{u}_{bulk,||}$, \mathbf{u}_{drift} , and u_{\perp} shown. The measured velocity vectors along the ring are indicated with black arrows (u_i), and the extent of the partial ring corresponds to the gray part of the ring. Panel (b): Velocity vectors measured by ICA and IES in ICA instrument coordinates (at 02:22 on 19 April 2016). The ring fitted to both datasets is shown in red, and the darker part marks the estimated extent of the partial ring.

to 360°. To find the extent of the partial ring, we take 100 equally spaced points of the fitted ring and map each velocity vector onto the closest sampled point. We use the same weighting as used for the ring fits and search for the shortest arc that contains 80% of the weighted sum of all the data points. For each scan (i.e., with the highest time resolution possible), we find the start and stop points of the arc using an iterative process. With this method, the extent of the partial ring is always underestimated. However, the chosen threshold value of 80% provided excellent results in terms of robustness and efficiently excluded noise and other small signals not connected to the partial ring, while keeping the underestimation to a minimum.

4. Results

In this section, we will focus on the plasma observations on 19 April 2016. This day shows signatures of a partial ring distribution of solar wind protons. To set this into the context of typical solar wind behavior during this time period, we also showcase a reference case on 23 April 2016.

4.1. 19 April 2016

The heliocentric distance on nineteenth of April 2016 was 2.8 AU. The distance of Rosetta to the comet nucleus was almost constant throughout the day, averaging at around 31 km. The level of cometary activity was around $5 \times 10^{25} \text{ s}^{-1}$ (derived from COPS data assuming isotropic outgassing) in the morning, and increased slightly in the afternoon.

4.1.1. Overview

Figure 2 shows Rosetta ion observations, plasma density, and magnetic field data. The top three panels show the energy-time spectrograms of ions as measured by ICA, split up into protons, alpha particles, and heavy ions. In the beginning of the day, protons (panel a) are observed with energies between 300 eV/q and 2 keV/q. Two types of structures appear during this time. Around 08:00 (all times are UT) protons continuously populate this entire energy range, resulting in one broad energy band. At 10:00, on the other hand, two separate energy bands can be identified. The differential fluxes of the two energy bands are usually different and one of the bands even disappears at times (e.g., at 07:00). The transitions between one single energy band and two separate ones happen

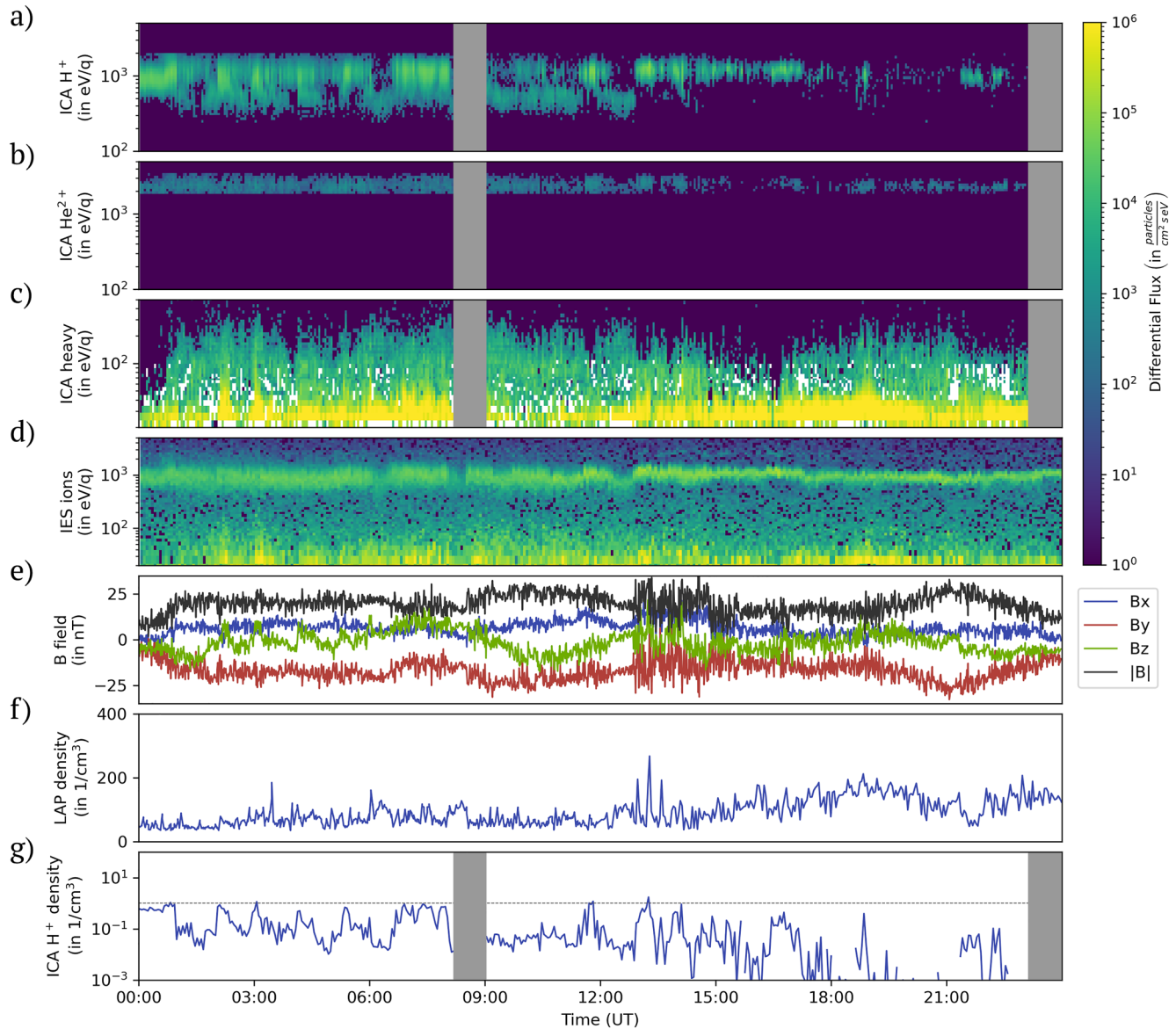


Figure 2. Timeseries overview of the nineteenth of April 2016. Panels (a)–(c) show the ion differential flux per Elq as measured by ICA, mass-separated into protons, alphas, and heavy ions. Panel (d) shows the ion differential flux per Elq as measured by IES. The differential flux colorbar is the same for panels (a)–(d). Panel (e) shows the magnetic field data as measured by RPC-MAG (in nT). The individual lines show the magnitude of the B -field and its individual components in a CSEQ reference frame. Panel (f) shows the plasma density, measured by LAP, and panel (g) shows the proton density, derived from ICA (both in cm^{-3}). The dashed line in panel (g) marks a density of 1 cm^{-3} . For the gray areas there is no ICA data available.

suddenly, within a few scans. At around 13:00, there is a transition to a more narrow energy band and even this band sometimes disappears completely. This is a field-of-view effect and will be discussed in the next section. Contrary to the ICA proton measurements, the alpha particles (panel b) were only observed in one energy band centered around 2.3 keV/q throughout the interval. In the afternoon, the signal sometimes disappears due to the same field-of-view effects mentioned above. The heavy ions (panel c) can be split into two parts: the newly ionized low energy ions (energies below 40 eV/q) are present the entire day, but show increased fluxes in the afternoon. At higher energies we see ions that have been accelerated by the solar wind electric field. These pickup ions are observed most of the time, but the differential flux and maximum energy for this ion population drop in the afternoon, especially around 16:00.

Panel d shows the IES ion observations. As IES is not mass-resolving all ion species are present. The overall behavior of the protons (signal band at 1 keV/q) is similar to ICA observations, with a broader energy distribution

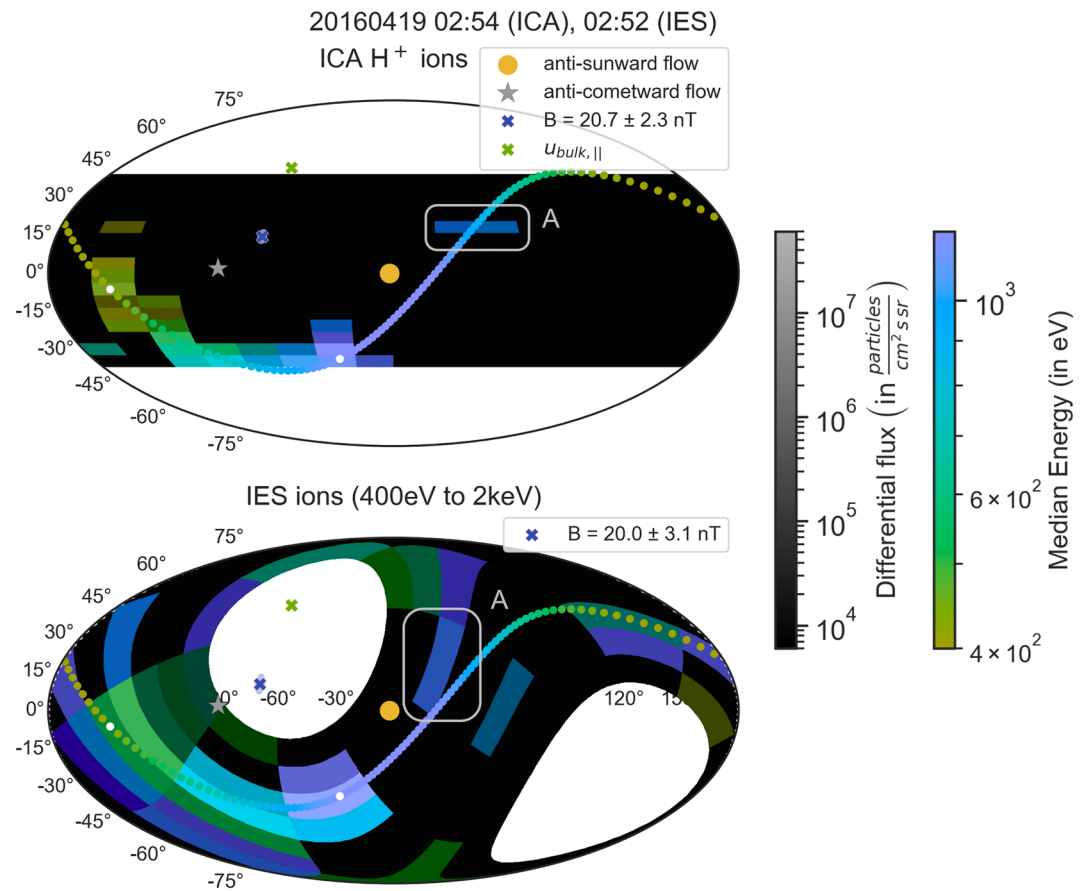


Figure 3. Azimuth-Elevation plots of ICA (upper panel) and IES (lower panel) for one individual instrument scan of each instrument. Elevation is shown by the left-hand axis, and azimuth ranges from -180° on the left to 180° on the right side. The partial ring structure with a decreasing energy along the ring can be seen in both instruments. The dotted line shows the fitted ring, color-coded using the same energy scale as the median energy for each pixel. The estimated start and end point of the partial ring are indicated with white dots. The gray boxes marked with A highlight a signal that is disconnected from the rest of the partial ring. More information can be found in Section 4.1.2.

in the morning compared to the afternoon. However, the signal in the morning does not split up into two energy bands at any point. In the afternoon no discontinuities are observed. At energies below 200 eV/q signatures of cometary pickup ions can also be seen throughout the entire day.

The magnetic field (panel e; magnitude, and components in CSEQ coordinates) has an average strength of 20.9 nT between $01:00$ and $13:00$ with little variation in amplitude and a dominating y-component. Only the z component shows changes of up to $\pm 10 \text{ nT}$, including sign changes, which does not have a large impact on the magnitude. After $13:00$ the fluctuations increase for all components.

The plasma density, as measured by LAP (panel f), is around 70 cm^{-3} in the morning but increases to an average value of 120 cm^{-3} in the afternoon, which is also reflected in the ICA measurements of low energy cometary ions (panel c), which are dominating the plasma at this time.

The proton density derived from ICA measurements (panel g) varies greatly throughout the entire day, but some features can be observed: the highest measured value is at around 1 cm^{-3} in the beginning of the day, and decreases in the afternoon (see dashed line at 1 cm^{-3}). The periods in the morning where the density drops correspond to the appearance of two energy bands in the energy spectrum. Density estimates from ICA often have large uncertainties, but our focus here is on the variations in the proton density rather than absolute numbers.

4.1.2. Angular Plots

In this section we use the method described in Section 3 to visualize the angle-energy dispersion of protons and alpha particles, and their relation to the magnetic field. To identify and compensate for possible field-of-view

effects we use both ICA and IES data for the protons. All angular plots cover single scans, so they show the data at the highest time resolution available for this day. The time resolution of ICA and IES differs, and we show the IES scan with the starting time closest to the starting time of the ICA scan. To make it easy to combine the two datasets, the IES data are rotated into the ICA coordinate system. When comparing the upper and lower panel of Figure 3, the complementary field-of-view of the two instruments is obvious.

Figure 3 shows a representative scan, taken around 02:54. At this time, we see very broad energy bands in both the ICA and IES ion spectra (see Figure 2, panels a and d). The upper panel of Figure 3 shows the median energy and differential flux of ICA protons. On the lower panel, IES ion data between 400 eV and 2 keV are displayed in the same manner. Both panels also show the anti-sunward and anti-cometward flow direction (yellow disc and gray star). Ions flowing from the Sun or the comet would be seen at the marked locations. The blue cross marker indicates the direction of the magnetic field, averaged over the entire scan. The underlying ellipse gives an estimate of the variability of the magnetic field direction during this scan.

We note that the ICA data set shows a large angular spread of the proton distribution along a continuous line at negative elevation angles. The median energy is the highest (1.2 keV) for the pixels closest to the anti-sunward direction and decreases down to 500 eV for the most deflected protons. The differential flux is similar for most pixels and only falls off for the most deflected protons. The broad spectra seen in Figure 2a reflects this energy dispersion. IES data have higher noise levels, but in the pixels with the highest fluxes, the same features as are seen in ICA data can be identified.

The observed distributions resemble partial rings, so we combine ICA and IES measurements into a single data set and apply the ring fitting method described in Section 3.2 in order to characterize the shape of the proton distribution. The resulting fitted ring for this scan is identical for both instruments and overlaid in both panels. It features the same energy scale as the data. We conclude that the shape of the ring and the energy dispersion match the data very well. The estimated direction of the parallel component of the bulk velocity direction ($\mathbf{u}_{\text{bulk},\parallel}$) is displayed with a green cross and deviates only about 30° from the magnetic field direction. The method to find the extent of the ring is described in Section 3.2.1. The white dots on top of the fitted ring indicate the estimated start and end of the partial ring. We note the slight underestimation of the partial ring extent, an effect of the method used.

In both panels, there is a signal deflected in the direction opposite to the rest of the distribution (positive elevation angles). The fluxes are lower and the angular spread is less, but this signal appears in many scans in similar position and energy range, and it is hence considered to be a real signal. It is highlighted by the gray box and marked with the letter A in Figures 3 and 4.

The magnetic field does not drastically fluctuate between 01:00 and 13:00, but it still sometimes exhibits changes on the timescale of individual scans. Figure 4 shows such a case. During three consecutive scans, the magnetic field magnitude is almost constant while the average direction changes by 32° . The change in the elevation angle from 25° to 8° is observable in Figure 4. During these three scans, we also see a change in the angular distribution of the protons. In the first scan, the ICA measurements (upper left panel) show a continuous partial ring close to the lower edge of the field of view. The IES measurement agrees well with this observation. In the next two scans, the entire proton distribution appears shifted downwards in elevation. Due to the higher angular resolution, this shift is more obvious in ICA data but can also be seen in IES data. As a result, the middle part of the partial ring with energies around 700 eV is not observed by ICA because it falls outside the field-of-view. However, the IES data suggest that plasma with these energies is still present. We conclude that the two separate energy bands, we observe in Figure 2, are a consequence of part of the distribution being outside of the ICA field-of-view.

With the change in B-field toward lower elevations, $\mathbf{u}_{\text{bulk},\parallel}$ also decreases in elevation. The angle between the B-field and $\mathbf{u}_{\text{bulk},\parallel}$ increases from 27° to 29° , which is small compared to the overall change of magnetic field direction. $\mathbf{u}_{\text{bulk},\parallel}$ is consistently observed at higher elevations compared to the magnetic field direction. The variability of the B-field direction during one scan is approximately 10° , which is much smaller than the difference between the $\mathbf{u}_{\text{bulk},\parallel}$ and the direction of the B-field. We make two important observations.

1. A change in the measured magnetic field direction coincides with a matching shift of the partial ring distribution.
2. The difference between the magnetic field direction and the estimated $\mathbf{u}_{\text{bulk},\parallel}$ cannot be explained by uncertainties due to the fitting procedure nor the variability of the magnetic field during one scan.

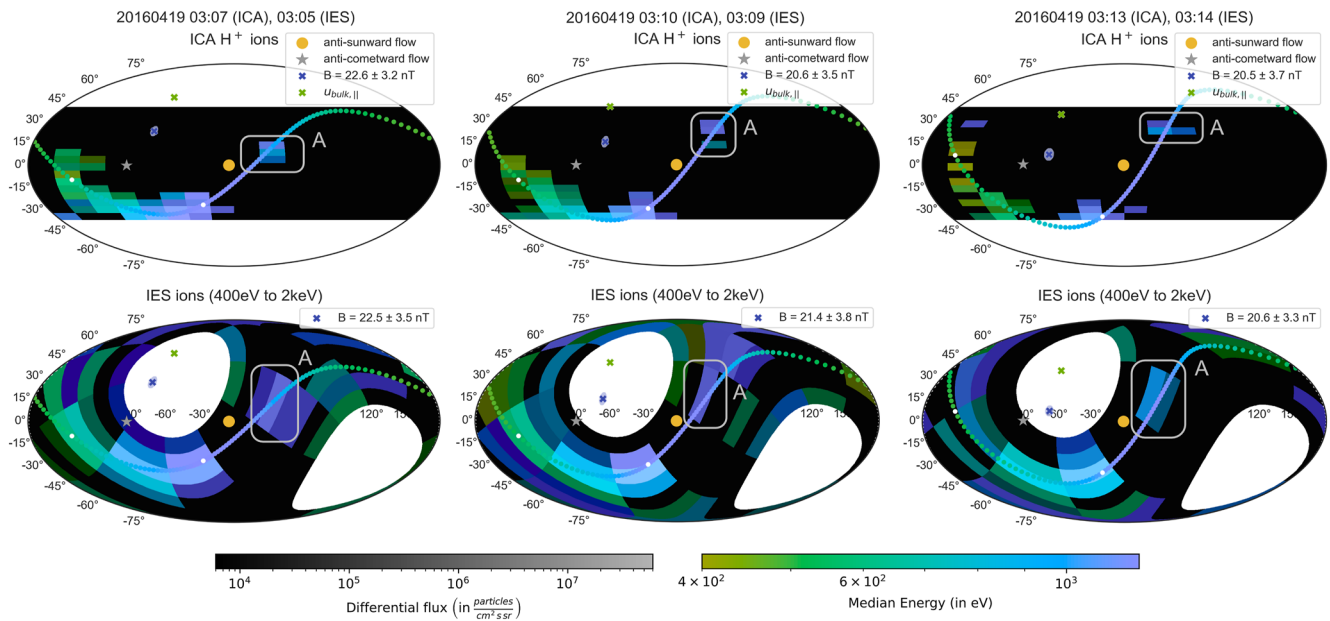


Figure 4. Azimuth-Elevation plots of three consecutive ICA- and IES-scans showing the response of the partial ring distribution to a change in B-field direction. The format is the same as described in Figure 3.

So far, we have only shown the angular distribution of protons. To get a complete picture of how the solar wind behaves, a comparison of protons (upper panel) and alpha particles (lower panel) of a single scan is given in Figure 5. Separate scales for both median energy and differential flux on the dual colormaps are used to account for the different plasma properties of the two species. Compared to the protons, the alpha particles are much less spread in angular space and also less deflected from the anti-sunward direction. There is a slight energy-angle dispersion visible in the scan shown in Figure 5, but such dispersion is not consistently observed during the day. Analysis of all scans between 01:00 and 13:00 shows that the angular spread of alpha particles never exceeds five pixels in elevation, and is rarely broader than two sectors in azimuth direction. The differential flux also falls off significantly for the two pixels at lowest elevations. Hence, we can exclude the possibility of field-of-view effects cutting away significant parts of the signal.

Due to the low fluxes of alpha particles and the lack of mass separation, it is difficult to use IES to confirm the observations mentioned above. Whenever there was a strong signal standing out in the IES data in the energy range between 2 and 4 keV, the observations match the ICA alpha particle data.

4.1.3. Timeseries of Fitted Rings

For a more comprehensive analysis of the partial rings, we applied the fitting procedure to all ICA and IES scans between 00:00 and 13:00, the time period when we observe the partial rings. There are 225 ICA scans available during this time, and the resulting fits were evaluated individually by visual inspection to exclude unsuccessful fits due to high noise in the data. This resulted in 180 good fits, a success rate of 80%. It is interesting to note that the success of the fitting procedure, as well as the resulting fit parameters, is not affected by the field-of-view limitations of the instruments.

A timeseries of the fitted parameters is given in Figure 6. Panel a shows the fitted ring velocities. The dominating velocity component is the gyration speed. It is relatively constant, with an average of $u_{\perp} = 362 \text{ km s}^{-1}$. The drift speed is also relatively constant, and averages at $u_{\text{drift}} = 98 \text{ km s}^{-1}$. The parallel component of the bulk velocity shows more variability, and extends from 0 up to 198 km s^{-1} . The average is $u_{\text{bulk},\parallel} = 51.5 \text{ km s}^{-1}$. The estimated ring angle extent (shown in panel b) fluctuates slightly over these 13 hr, ranging from 90° to 150° . Apart from a slightly smaller angle in the beginning of the day, there is no clear trend, and the average ring extent is 111.4° . In panel c, we show the angle between the magnetic field and $\mathbf{u}_{\text{bulk},\parallel}$. It drops from above 60° early in the morning to 10° around 6:00, and remains low for the next 2 hr. Between 9:00 and 13:00, the magnetic field direction and $\mathbf{u}_{\text{bulk},\parallel}$ deviate significantly, and the average angle is 38° .

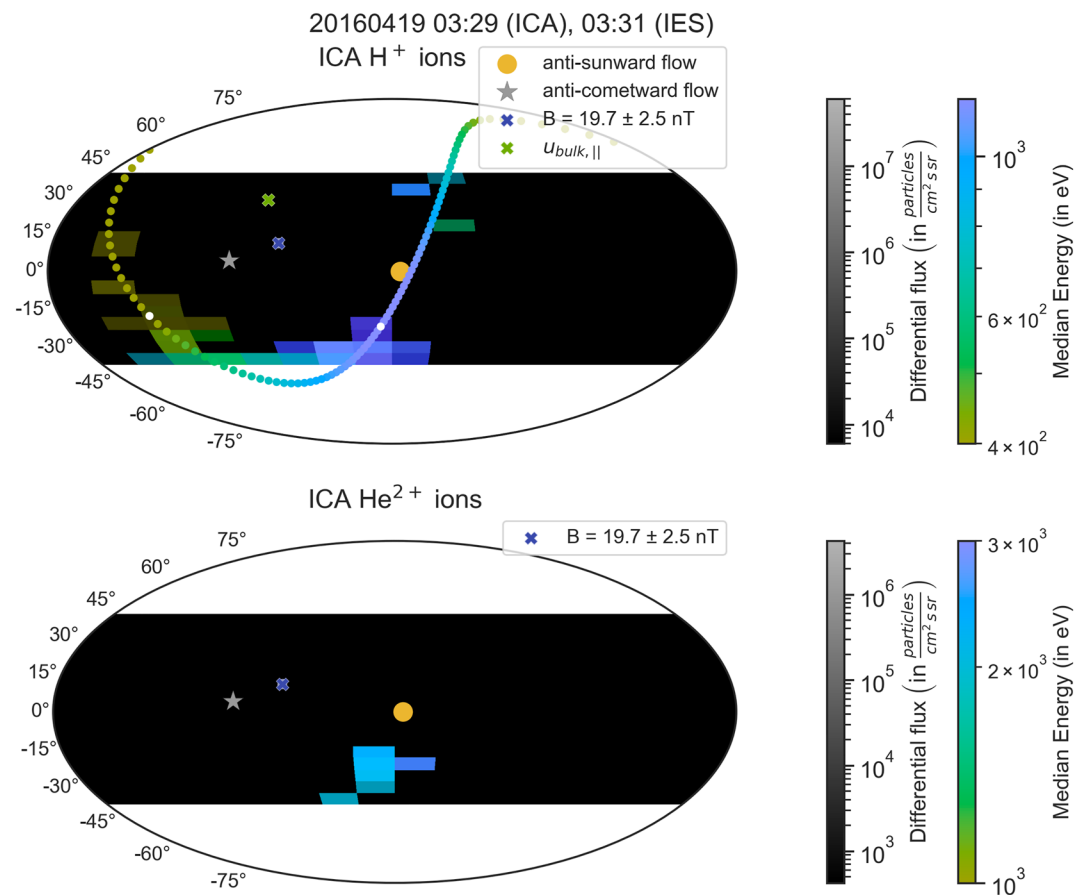


Figure 5. Azimuth-elevation plots of SW protons (upper panel) and alphas (lower panel) as measured by ICA. The alpha particles exhibit no prominent ring features and are in general less deflected than the protons. The format of the upper panel is the same as in Figure 3. The color bars in the lower panel are adjusted to match the different flux and energy range of the alpha particles compared to protons.

4.2. Reference Case

As a reference case, we choose 23 April 2016. Since it is only 4 days later than our main case, the heliocentric distances are comparable, as is the distance of Rosetta to the nucleus (around 30 km). However, the production rate for the reference case is about four times as high, with an average of $2.1 \times 10^{26} \text{ s}^{-1}$.

4.2.1. Overview

Figure 7 shows the same plasma parameters as Figure 2 but for the reference case. The ICA proton measurements (panel a) show a narrow energy band with a center energy around 600 eV/q, constant throughout most of the day. Only between 14:15 and 15:30, and after 19:30, there is an increase in the center energy of the energy band, along with slight broadening and an increase in differential flux. The alpha particles (panel b) appear as a barely visible narrow band with a center energy of 1.3 keV/q. The differential fluxes are barely above the detection threshold of the instrument. During times where there is no signal available, for example, at 5:00, the particle fluxes are probably too low to be detected by ICA. The ICA heavy ion spectrum (panel c) is dominated by low energy cometary ions. Pickup ions can be seen between 14:15 and 15:30, and after 19:30, but the fluxes are much lower compared to the main case. The proton signatures in IES (panel d) are very faint or not available during this day, mostly due to field-of-view effects. There are also no traces of cometary pickup ions visible in the IES data.

Magnetic field measurements (panel e) show a calm magnetic field with an average magnitude of 10.5 nT. There is a slight change in direction over the course of the day, as seen in the x - and y -components. The z -component only shows large changes between 14:15 and 15:30. The LAP estimate of the plasma density (panel f) increases from 100 cm^{-3} in the beginning of the day to above 300 cm^{-3} in the afternoon. As in our main case the density is

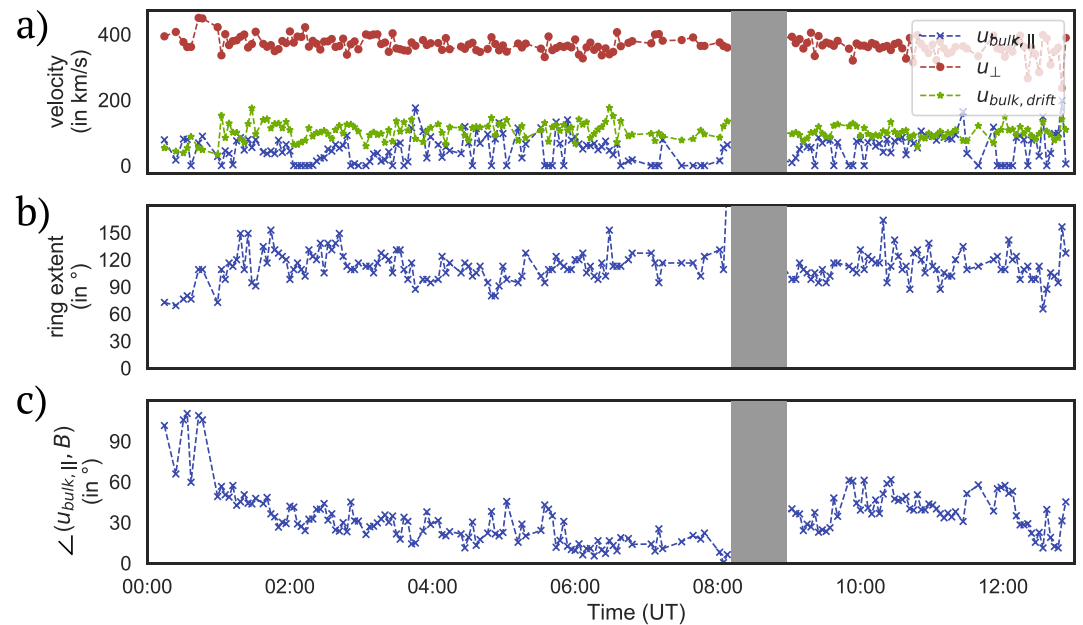


Figure 6. Timeseries of fitted ring parameters (19 April 2016). Panel (a) shows the magnitude of the fitted velocities $\mathbf{u}_{\text{bulk},\parallel}$, $\mathbf{u}_{\text{drift}}$, and u_{\perp} in km/s. Panel (b) shows the estimated extent of the ring angle. Panel (c) shows the angle between the vectors of the locally measured magnetic field direction \mathbf{B} and the fitted parallel velocity direction $\mathbf{u}_{\text{bulk},\parallel}$. Only successful fits are included in the timeseries. No ICA data are available for times within the gray area.

dominated by low energy cometary ions. The proton density (panel g) is around 0.1 cm^{-3} most of the time, with the exception of the time between 14:15 and 15:30, where it has a plateau at a value of 0.5 cm^{-3} .

4.2.2. Angular Plots

The angular spread of the protons for the reference case is much smaller than in the partial rings case, and appears beam-like instead of ring-shaped (Figure S1 in Supporting Information S1). The beam is less deflected than what was observed for the partial rings, and the magnetic field configuration differs in both magnitude and direction. There is also no clear angle-energy dispersion visible. A typical example of flow directions of alphas and protons for the reference case is shown in Figure S1 in Supporting Information S1).

The alpha particle distributions are very similar to both the proton distributions in this case, as well as the alpha particle distribution of the partial rings case, only with a lower flux. In fact, the differential flux is so low that it is just above the detection threshold of the instrument for this energy range, which explains the lack of a continuous alpha signal band in Figure 7 (i.e., whenever the fluxes drop just slightly, they will not be detected by ICA). As in the partial rings case, the angular deflection of alpha particles is less than for protons.

4.3. Proton Temperatures

The broad energy band seen in Figure 2a, with a spread of 1 keV, gives the impression of a heated proton population. At 1 AU the mean proton temperature is 12.7 eV (Wilson et al., 2018), and decreases with $T \sim R^{-0.3}$ (cf. Belcher et al., 1981) to an expected solar wind proton temperature of 9 eV at 2.8 AU. Figure 3 reveals that the width of the spectrum is a result of an energy-angle dispersion rather than heating. In this context, we define heating as an irreversible process resulting in an increased temperature. The proton temperature would correspond to the width of the ring in velocity space, which is hard to determine from the data with the given angular resolution. Instead we assume an isotropic temperature and fit a Maxwellian to the energy distribution observed in each individual pixel that contains a measurable differential flux. We require five non-zero values in the energy distributions to fit and each scan typically contains 5–15 pixels where a fit can be made. All fits are visually inspected and bad fits are removed. Figure 8 shows the fitted temperature, expressed as the thermal velocity versus the bulk velocity (obtained from the same fit). The thermal velocities correspond to energies in the range 5–20 eV. The color of each dot is the modified index of agreement, a measure of the goodness of fit (Willmott, 1981). In

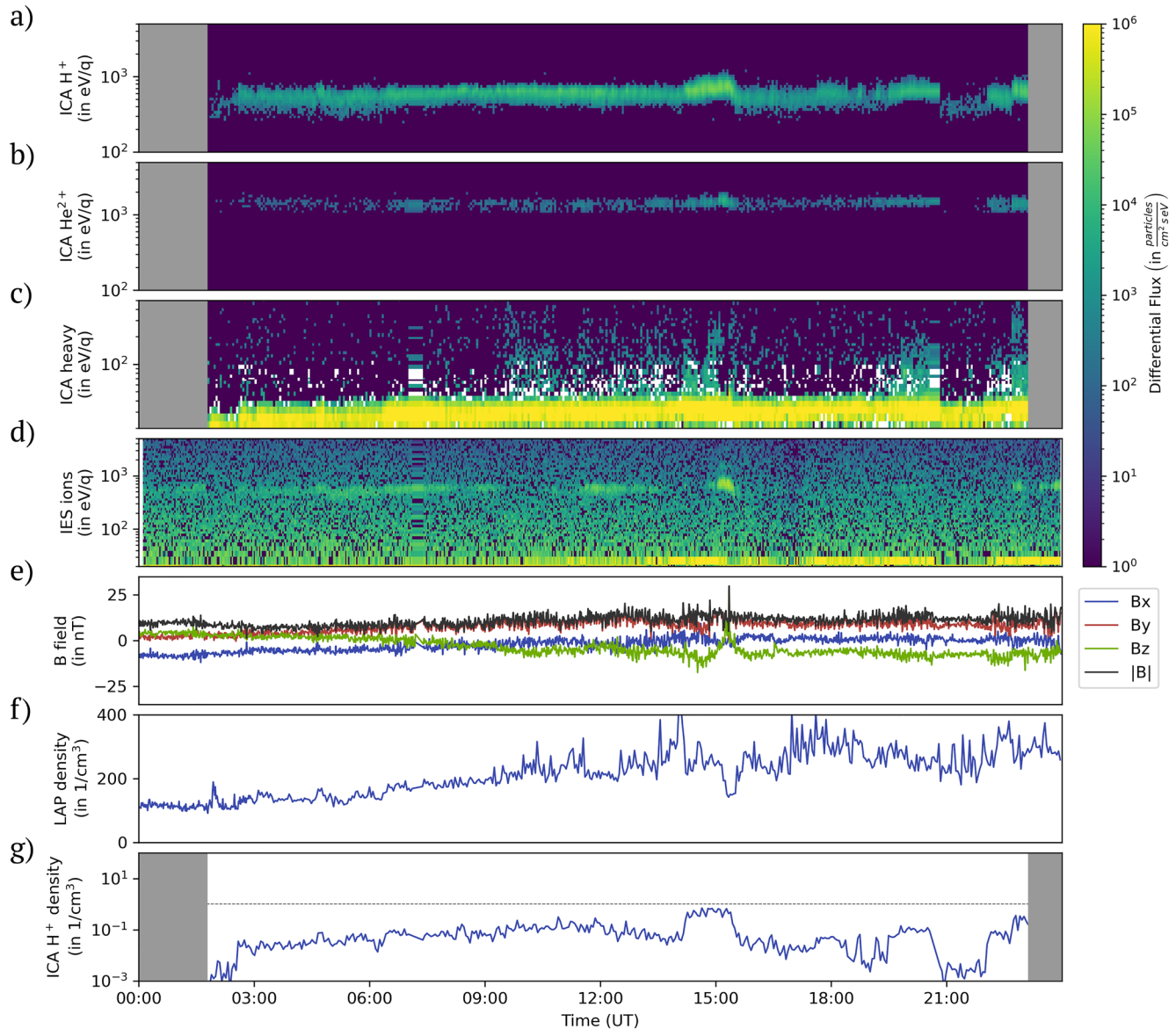


Figure 7. Timeseries overview of the 23rd of April 2016. The format is the same as described in Figure 2.

Figure 8, we use the first 30 of the 180 good scans identified in Section 4.1.3 to get a representative view of the distribution. We note a clear dependence, and a linear fit is a reasonable representation of the data. We could not identify any reason why the method used should generate this dependence. The Pearson correlation is 0.65.

For the reference case we obtain most of the proton temperatures between a few eV and about 15 eV, with no obvious correlation between the thermal and bulk velocities (not shown). We note though that bulk velocity is almost constant and hence it is difficult to determine any dependence.

5. Discussion

To put the partial ring observations into a global context of the cometary environment, we compare with model results. Visualizing the model results requires a projection into a coordinate system. Most useful for our case is the projection into magnetic coordinates centered at the comet, where the x -axis is in the sunward direction, which corresponds to $-\mathbf{v}$ of the undisturbed solar wind. The y -axis is along the solar wind magnetic field direction perpendicular to \hat{x} . The z -axis completes the right-handed system, and is along the convective electric field

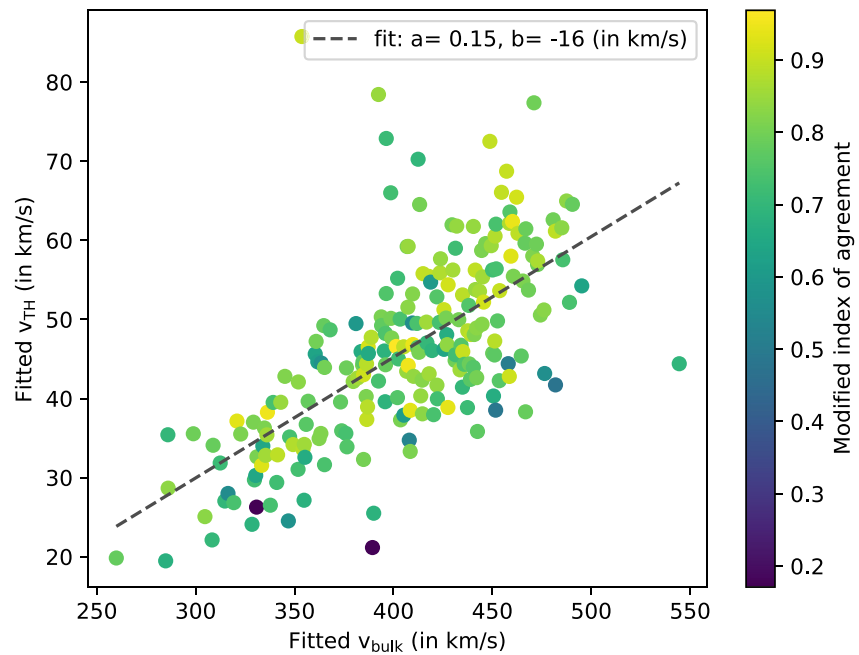


Figure 8. Fitted proton thermal speed as a function of the bulk speed obtained from the same fit. The goodness of fit (modified index of agreement; Willmott, 1981) is color-coded and all fits have been inspected manually. A low modified index of agreement corresponds to cases where the flanks of the distribution do not perfectly match a Maxwellian.

($\mathbf{E} = -\mathbf{v} \times \mathbf{B}$). This separates the comet environment into two hemispheres, referred to as $+E$ ($z > 0$) and $-E$ hemisphere ($z < 0$), respectively. The terminator plane at $x = 0$ is the orbit plane of Rosetta for both days discussed in this paper.

Only few models focus on the specific case of low cometary activity and resolve the low distance between Rosetta and comet 67P. One such model is presented in Gunell et al. (2018) for a heliocentric distance of 2.4 AU. It predicts the formation of a solar wind proton density enhancement layer draping asymmetrically around the nucleus, and continuing in the tail region in the $-E$ hemisphere. In the terminator plane this density enhancement layer coincides with a local enhancement of the magnetic field strength, as well as a broadening of the proton energy spectra. At the same time the alpha particles appear as almost undisturbed solar wind. The model by Gunell et al. (2018) further shows a $+E$ hemisphere characterized by the occurrence of cometary pickup ions with energies exceeding 100 eV. Many of the features of the model correspond to our observations: the broadened proton energy spectra with increased density, an increased magnetic field strength, and the occurrence of energetic pickup ions are all present during the observations of the partial rings. In a continuation of this study that surveys proton spectra of the entire mission, Goetz et al. (2021) find over 300 cases of warm protons that they identify as indicative of this plasma boundary. The partial rings case presented here coincides with one of the events reported in their study. This is not surprising, as the main characteristic feature of both studies is a broad distribution of the proton energy spectra. However, we have shown that the observed broadening of the energy spectra in our case is mainly due to the energy-angle dispersion of the protons, and not due to an increase in temperature in the plasma reference frame. This makes a model with a more detailed analysis of the flow directions very useful.

The 2D kinetic model from Behar et al. (2018) provides a simplified view of the trajectories of solar wind protons. They assume that the neutral gas density of the comet falls off as $1/r^2$, and that the amplitude of the magnetic field is proportional to $1/r^2$ as well. Because no electric field is included in the model, particles are only gyrating and do not change energy. Consequently, changes in the gyroradius are only due to a change in cometocentric distance, and not due to the convective electric field or a change in particle speed. In this semi-analytical model, the solar wind—modeled containing only a proton population—gets deflected around the comet in an asymmetric manner. The results were verified with a hybrid model, and show a similar density enhancement layer compared to that in Gunell et al. (2018). The region cometward of this layer is depleted of solar wind ions. In the

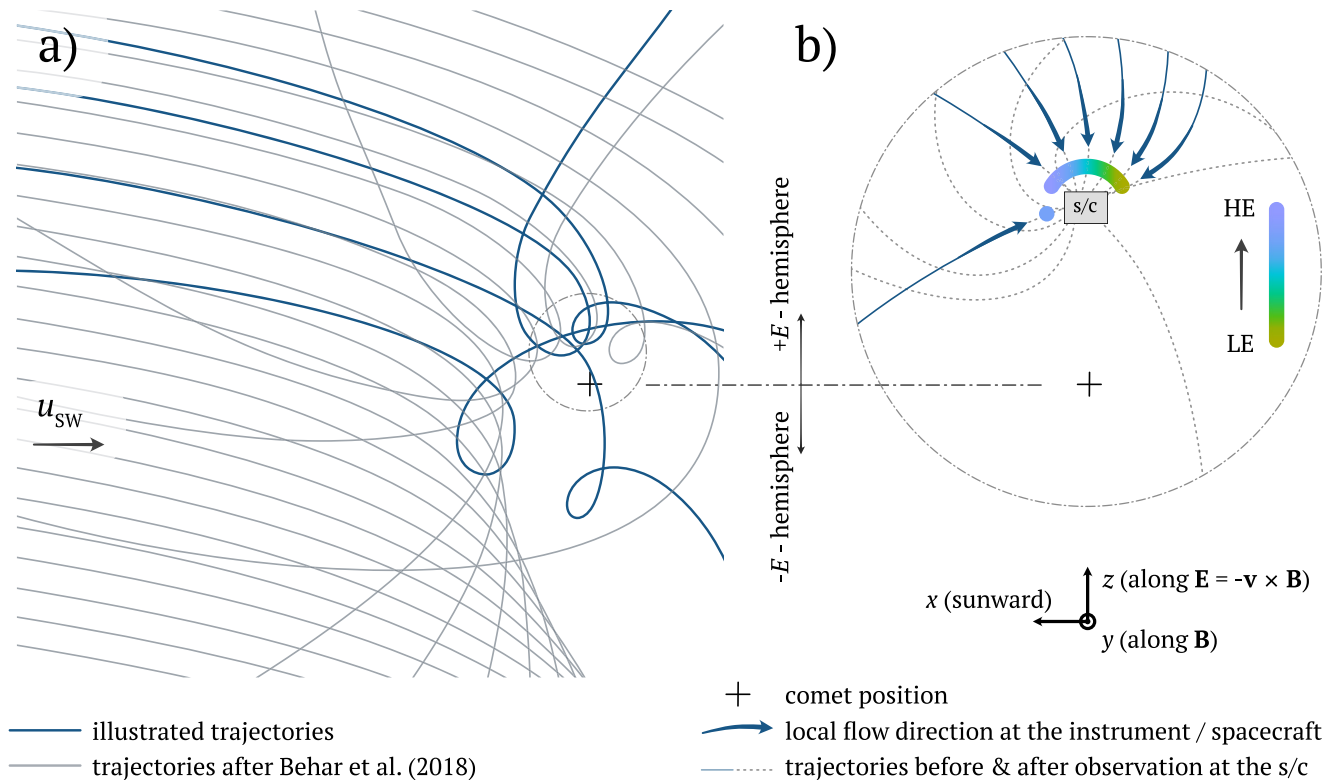


Figure 9. Illustration of the solar wind proton trajectories leading to partial ring distributions at comet 67P for low activity. Panel (a) shows a global view. The illustrated trajectories are shown in blue. The theoretical trajectories from the kinetic model (after Behar et al. (2018)) are underlaid in gray. Panel (b) shows a local view, with the flow direction of the protons at the spacecraft indicated by the arrows, and the continuation of the trajectories drawn with dotted lines. The change in energy of the observed protons depending on the arrival direction is indicated with a color bar that increases from low (LE) to high (HE) energies (same as e.g., Figure 3). The undisturbed solar wind flow direction is shown on the left side (u_{SW}). In both panels the separation into a +E and -E hemisphere is indicated.

+E hemisphere, the density enhancement is only visible close to the nucleus, and dominated by highly deflected, almost sunward-streaming ions. Assigning spatial scales to the dimensionless model places the density enhancement at about 12 km in the +E hemisphere for a heliocentric distance of 3 AU (Behar et al., 2018). However, this value strongly depends on the comet plasma parameters, such as the outgassing rate, and the upstream solar wind conditions. Thus, typical values for a given heliocentric distance may change by a factor of two or more depending on the specific plasma environment.

We used the particle trajectories of both the kinetic model and the hybrid model shown in Behar et al. (2018) (cf. their Figure 7) to create a sketch of possible flow patterns of solar wind protons. Figure 9a shows some suggested solar wind proton trajectories (blue lines), partially based on the hybrid simulation results presented in Behar et al. (2018) for a low cometary activity. The theoretical trajectories from the kinetic simulation are shown in gray, and the density enhancement region is visible. The illustration is kept free of spatial scales, but represents the low-activity case where a density enhancement region would be found a few tens of km away from the nucleus in the +E hemisphere. The exact value depends on the comet outgassing and the upstream solar wind parameters. As mentioned above, the kinetic model does not include any electric fields. Consequentially, the solar wind does not necessarily retain a significant anti-sunward drift component as imposed by the convective electric field. In addition to that, a gyration in a convective electric field will also decrease the particle velocity on parts of its trajectory. This will lead to a further decrease of the gyroradius, especially close to the nucleus where the deflection is the most significant. Our illustration of the trajectories attempts to include the effects of a convective electric field as well as asymmetries in the outgassing. This results in more cycloidal trajectories compared to the kinetic model, and a more diverse flow pattern. We see that even a slight perturbation from the simplified case creates a highly complex interaction region in the +E hemisphere. The density enhancement layer observed here is a focal point for ion trajectories coming from different directions, with the largest angular range of the proton flow directions occurring in the +E hemisphere. Here, the different proton trajectories would be observed as a partial

ring. The spatial extent of the focal region is small, which requires the spacecraft to be located in a very specific region for these rings to be seen. This result goes beyond the highly deflected, but still beam-like monoenergetic distribution of solar wind protons along the caustic, as presented in Behar et al. (2018).

In Figure 9b, a local view of the illustrated trajectories near the comet and the spacecraft is shown. The solid lines and arrows indicate the flow pattern of ions before intersecting at the observation point. Their trajectories after the observation point are shown by the dashed lines. The flow directions vary from slightly deflected anti-sunward to an almost sunward flow. The change in energy in the comet reference frame is due to the gyration of the solar wind protons around the center of mass of the bulk plasma reference frame, estimated by the fitted ring parameters $\mathbf{u}_{\text{bulk},\parallel}$ and $\mathbf{u}_{\text{drift}}$. Because of the negligible speed of Rosetta relative to the comet nucleus, the comet reference frame is also the spacecraft reference frame. The ions moving in an anti-sunward direction will have the highest energies, while the more deflected ones exhibit lower energies in the comet reference frame. This relation is illustrated using the same energy colorbar as in the dual colormap plots (see e.g., Figure 3). For the case that a particle performs a nearly full gyration before being observed, the energy is expected to be similar to the only slightly deflected solar wind. Such a signal has been consistently observed along with the partial rings, although with a lower flux intensity (see Figure 4, at 30° elevation near the anti-sunward flow direction in all three panels).

What information can we obtain from these partial ring observations? The estimated parameters $\mathbf{u}_{\text{bulk},\parallel}$ and $\mathbf{u}_{\text{drift}}$ describe the average gyration center of the solar wind protons. In a generalized description of different ion populations, $\mathbf{u}_{\text{drift}}$ is the same for the entire plasma population (assuming an $\mathbf{E} \times \mathbf{B}$ drift). The direction of the parallel component $\mathbf{u}_{\text{bulk},\parallel}$ provides a proxy for the average magnetic field direction in the entire interaction region of the ions observed as partial rings. A comparison between this proxy and the local magnetic field direction measured by MAG, as seen in Figure 6 in the second panel, provides information about the differences between the local and the average global +E hemisphere upstream of the observation point. At large distances from the nucleus, the direction of the magnetic field is expected to be similar to that of the undisturbed solar wind (Goetz et al., 2017). Only close to the nucleus (<50 km), magnetic field draping becomes important (Koenders et al., 2016). We also estimate the gyration speed u_{\perp} of the protons. This gyration speed carries the kinetic energy that is no longer in the bulk plasma drift of the protons. Due to the similar spatial scales of the ion gyroradii (approximately 180 km for protons at the spacecraft) and the comet environment the gyration motion is still in its initial stage. As the scale size of the interaction grows significantly larger than an ion gyroradius, it is likely that this gyration will evolve into increased thermal velocity via heating processes (Coates & Jones, 2009). In such a comet environment, a shock is likely to form.

To verify that Rosetta was in the +E hemisphere when we observed the partial rings, we used the direction of $\mathbf{u}_{\text{bulk},\parallel}$ to define the y-axis of the magnetic field coordinates. From this, we determined that the spacecraft is located in the +E hemisphere (see Figure S2 in Supporting Information S1). Using the local magnetic field measurements for the coordinate transformation instead resulted in a larger spread of the spacecraft position. This indicates that $\mathbf{u}_{\text{bulk},\parallel}$ is indeed a better estimate for the average upstream magnetic field direction than the local magnetic field measurements.

During the reference case, Rosetta was also located in the +E hemisphere, at a similar radial distance to the comet nucleus as in the partial rings case. However, the outgassing rate of the comet during that day was higher, as seen, e.g., in the LAP and COPS densities. This is likely due to a latitudinal effect of the comet activity (Hansen et al., 2016). A higher outgassing rate will lead to a density enhancement layer that is further away from the comet under identical solar wind conditions, and we conclude that Rosetta was likely located cometward of the density enhancement layer during the reference case. This is supported by the observed lower solar wind proton density and the reduced angular spread with no energy dispersion. The only slightly deflected solar wind is similar to what is expected further upstream. A density enhancement layer at such small spatial scales compared to the ion gyroradius seems to create a boundary that is partially permeable by the solar wind. A solar wind ion cavity does not form, which is in agreement with hybrid simulations (Koenders et al., 2016).

There is a time period between 14:15 and 15:30 on the reference day that shows deviating properties. The proton densities are enhanced by about an order of magnitude, and an energy-angle dispersion is visible, along with a broadening of the energy spectra. In this time period we also observe a weak flux of pickup ions. We think that during this time, a change in the upstream solar wind conditions led to a compression of the density enhancement layer and pushed it closer to the spacecraft.

The temperatures of the individual pixels range between 5 and 20 eV in the partial rings case. Similar values, from a few eV to 15 eV, were observed in the reference case. The linear increase in proton temperature with the bulk velocity in the partial rings case is difficult to explain. Intuitively, a lower bulk velocity suggests more energy dissipation and heating but we observe the opposite. Either the heating is more efficient along direct paths (higher velocities) to the focus point, or the energy-angle dispersion results in an additional velocity filtering of the protons arriving there.

6. Conclusions and Summary

On 19th of April 2016, we observe an unusually broad signal in the proton energy spectra. We show that the broadening of the spectra in this case is due to an energy-angle dispersion of the solar wind protons, and not due to heating. This energy-angle dispersion manifests itself as a partial ring in velocity space. Rings are successfully fitted to the data providing estimates of the bulk flow properties and the gyration speed of the protons. The parallel component of the bulk flow $u_{\text{bulk},\parallel}$ provides an estimate of the average upstream magnetic field direction. The average gyration center of the solar wind protons obtained from the fit is an estimate of the bulk plasma speed of the entire plasma population of the interaction region. The gyration speed obtained from the fit corresponds to a transfer of kinetic energy from the bulk drift into a non-drifting motion, and may thus correspond to the initial stage of heating of the solar wind plasma when interacting with an obstacle, as has been observed at the Earth's bow shock (Morse, 1976; Skopke et al., 1983). The observations presented here provide more details of a plasma distribution that may represent the initial stage leading up to shock formation, as has been previously studied by Goetz et al. (2021) and Gunell et al. (2018).

Comparison with models shows that these partial rings can likely only be observed in the $+E$ hemisphere of the comet within a density enhancement layer. This density enhancement layer is a focal point where different solar wind proton trajectories converge. At this location the protons show a large spread in energy and direction, resulting in the observed partial rings. The observations are also characterized by enhanced solar wind proton densities, the occurrence of cometary pickup ions, and a strong magnetic field, and support the picture given by models. These partial ring observations are a stark contrast to the slightly deflected and beam-like solar wind that dominates our observations at large heliocentric distances and low cometary activity. Due to their larger gyroradii, alpha particles are only lightly deflected in both cases. The thickness of the density enhancement layer is small, and its distance to the nucleus depends on the comet activity and the solar wind conditions. Rosetta had to be at a very specific location to observe these partial rings, which makes the observations presented in this study rare.

Data Availability Statement

The data used in this study is available through the ESA Planetary Science Archive (ESA PSA) and NASA Planetary Data System (NASA PDS). For RPC-ICA, the mass-separated dataset (Nilsson, 2021a) and the derived moment data (Nilsson, 2021b) were used. The additional ion data is the calibrated data from RPC-IES (Trantham 2019). Magnetic field data (RPC-MAG) was obtained from Richter et al. (2019). For the electron density, we used the ned_density parameter from RPC-LAP (Eriksson et al., 2020). Spacecraft attitude and orbit data was obtained using SPICE kernels (Acton et al., 2018; ESA SPICE Service, 2019) and the Python implementation SpiceyPy (Annex et al., 2020). Data analysis was done using NumPy version 1.20.2 (Harris et al., 2020). Figures were made using Matplotlib (Caswell et al., 2021; Hunter, 2007) and Colorspacious (Smith, 2015).

References

- Acton, C., Bachman, N., Semenov, B., & Wright, E. (2018). A look towards the future in the handling of space science mission geometry. *Planetary and Space Science*, 150, 9–12. <https://doi.org/10.1016/j.pss.2017.02.013>
- Annex, A. M., Pearson, B., Seignovert, B., Carcich, B. T., Eichhorn, H., Mapel, J. A., et al. (2020). SpiceyPy: A Pythonic Wrapper for the SPICE Toolkit (Vol. 5) (software No. 46) [Software]. *The Open Journal*, 5(46), 2050. <https://doi.org/10.21105/joss.02050>
- Balsiger, H., Altwegg, K., Bochsler, P., Eberhardt, P., Fischer, J., Graf, S., et al. (2007). Rosina–Rosetta orbiter spectrometer for ion and neutral analysis. *Space Science Reviews*, 128(1), 745–801. <https://doi.org/10.1007/s11214-006-8335-3>
- Behar, E., Lindkvist, J., Nilsson, H., Holmström, M., Stenberg-Wieser, G., Ramstad, R., & Götz, C. (2016). Mass-loading of the solar wind at 67P/Churyumov-Gerasimenko. Observations and modelling. *Astronomy and Astrophysics*, 596, A42. <https://doi.org/10.1051/0004-6361/20168797>
- Behar, E., Nilsson, H., Alho, M., Goetz, C., & Tsurutani, B. (2017). The birth and growth of a solar wind cavity around a comet - Rosetta observations. *Monthly Notices of the Royal Astronomical Society*, 469(Suppl_2), S396–S403. <https://doi.org/10.1093/mnras/stx1871>

Acknowledgments

Rosetta is a European Space Agency (ESA) mission with contributions from its member states and the National Aeronautics and Space Administration (NASA). Work at the Swedish Institute of Space Physics in Kiruna (IRF) was funded by the Swedish National Space Agency (SNSA) Grants 132/19 and 2021-00105. Work at Umeå university was supported by the SNSA Grant 108/18.

- Behar, E., Tabone, B., Saillenfest, M., Deca, J., Holmström, M., Nilsson, H., et al. (2018). Solar wind dynamics around a comet - a 2D semi-analytical model. *Astronomy and Astrophysics*, 620, A35. <https://doi.org/10.1051/0004-6361/201832736>
- Belcher, J. W., Bridge, H. S., Lazarus, A. J., & Sullivan, J. D. (1981). *Preliminary results from the voyager solar wind experiment*. In H. Rosenbauer (Ed.), *Fourth Solar Wind Conference* (pp. 131–142). Springer-Verlag.
- Beth, A., Galand, M., Nilsson, H., Goldstein, R., Mokashi, P., Eriksson, A., et al. (2019). RPC user Guide version 3 (Vol. 9). Retrieved from <https://cosmos.esa.int/web/psa/rosetta>
- Burch, J. L., Goldstein, R., Cravens, T. E., Gibson, W. C., Lundin, R. N., Pollock, C. J., et al. (2007). Rpc-ies: The ion and electron sensor of the Rosetta plasma consortium. *Space Science Reviews*, 128(1–4), 697–712. <https://doi.org/10.1007/s11214-006-9002-4>
- Carr, C., Cupido, E., Lee, C. G. Y., Balogh, A., Beek, T., Burch, J. L., et al. (2007). Rpc: The Rosetta plasma consortium. *Space Science Reviews*, 128(1), 629–647. <https://doi.org/10.1007/s11214-006-9136-4>
- Caswell, T. A., Lee, M. D. A., de Andrade, E. S., Hunter, J., Hoffmann, T., Firing, E., et al. (2021). matplotlib/matplotlib: REL v3.4.1 [Software]. <https://doi.org/10.5281/zenodo.4649959>
- Coates, A. J. (2004). Ion pickup at comets. *Advances in Space Research*, 33(11), 1977–1988. <https://doi.org/10.1016/j.asr.2003.06.029>
- Coates, A. J., Johnstone, A. D., Wilken, B., Jockers, K., & Glassmeier, K.-H. (1989). Velocity space diffusion of pickup ions from the water group at comet Halley. *Journal of Geophysical Research*, 94(A8), 9983–9993. <https://doi.org/10.1029/ja094ia08p09983>
- Coates, A. J., & Jones, G. H. (2009). Plasma environment of Jupiter family comets. *Planetary and Space Science*, 57(10), 1175–1191. <https://doi.org/10.1016/j.pss.2009.04.009>
- Eriksson, A. I., Gill, R., Johansson, E. P. G., & Johansson, F. L. (2020). Rosetta RPC-LAP archive of derived plasma parameters from the Rosetta Extension 2 mission phase [Dataset]. ESA Planetary Science Archive and NASA Planetary Data System. Retrieved from <https://pdssbn.astro.umd.edu/holdings/ro-c-rplac-5-ext2-deriv2-v1.0/dataset.shtml>
- Eriksson, A. I., Boström, R., Gill, R., Åhlén, L., Jansson, S.-E., Wahlund, J.-E., et al. (2007). Rpc-lap: The Rosetta Langmuir probe instrument. *Space Science Reviews*, 128(1), 729–744. <https://doi.org/10.1007/s11214-006-9003-3>
- ESA SPICE Service. (2019). Rosetta SPICE Kernel Dataset [Dataset]. <https://doi.org/10.5270/esa-tyidsbudataset>
- Filacchione, G., Groussin, O., Hery, C., Kappel, D., Mottola, S., Oklay, N., et al. (2019). *Comet 67p/cg nucleus composition and comparison to other comets* (Vol. 215). Springer Netherlands. <https://doi.org/10.1007/s11214-019-0580-3>
- Glassmeier, K.-H., Boehnhardt, H., Koschny, D., Kürt, E., & Richter, I. (2007). The Rosetta mission: Flying towards the origin of the solar system. *Space Science Reviews*, 128(1–4), 1–21. <https://doi.org/10.1007/s11214-006-9140-8>
- Glassmeier, K.-H., Richter, I., Diedrich, A., Musmann, G., Auster, U., Motschmann, U., et al. (2007). RPC-mag the fluxgate magnetometer in the Rosetta plasma consortium. *Space Science Reviews*, 128(1), 649–670. <https://doi.org/10.1007/s11214-006-9114-x>
- Goetz, C., Behar, E., Beth, A., Bodewits, D., Bromley, S., Burch, J., et al. (2022). The plasma environment of comet 67p/Churyumov-Gerasimenko. *Space Science Reviews*, 218(8), 65. <https://doi.org/10.1007/s11214-022-00931-1>
- Goetz, C., Gunell, H., Johansson, F., Llera, K., Nilsson, H., Glassmeier, K. H., & Taylor, M. G. (2021). Warm protons at comet 67p/Churyumov-Gerasimenko-implications for the infant bow shock. *Annales Geophysicae*, 39(3), 379–396. <https://doi.org/10.5194/angeo-39-379-2021>
- Goetz, C., Volwerk, M., Richter, I., & Glassmeier, K. H. (2017). Evolution of the magnetic field at comet 67p/Churyumov-Gerasimenko. *Monthly Notices of the Royal Astronomical Society*, 469(Suppl_2), S268–S275. <https://doi.org/10.1093/mnras/stx1570>
- Gunell, H., Goetz, C., Simon Wedlund, C., Lindkvist, J., Hamrin, M., Nilsson, H., et al. (2018). The infant bow shock: A new Frontier at a weak activity comet. *A&A*, 619, L2. <https://doi.org/10.1051/0004-6361/201834225>
- Hansen, K. C., Altwegg, K., Berthelier, J. J., Bieler, A., Biver, N., Bockelée-Morvan, D., et al. (2016). Evolution of water production of 67p/Churyumov-Gerasimenko: An empirical model and a multi-instrument study. *Monthly Notices of the Royal Astronomical Society*, 462, S491–S506. <https://doi.org/10.1093/mnras/stw2413>
- Harris, C. R., Millman, K. J., van der Walt, S. J., Gommers, R., Virtanen, P., Cournapeau, D., et al. (2020). Array programming with NumPy. *Nature*, 585(7825), 357–362. <https://doi.org/10.1038/s41586-020-2649-2>
- Haser, L. (1957). Distribution d'intensité dans la tête d'une comète. *Bulletin de la Société Royale des Sciences de Liège*, 43, 740–750.
- Hunter, J. D. (2007). Matplotlib: A 2D graphics environment. *Computing in Science & Engineering*, 9(3), 90–95. <https://doi.org/10.1109/MCSE.2007.55>
- Koenders, C., Glassmeier, K.-H., Richter, I., Ranocha, H., & Motschmann, U. (2015). Dynamical features and spatial structures of the plasma interaction region of 67p/Churyumov-Gerasimenko and the solar wind. *Planetary and Space Science*, 105, 101–116. <https://doi.org/10.1016/j.pss.2014.11.014>
- Koenders, C., Perschke, C., Goetz, C., Richter, I., Motschmann, U., & Glassmeier, K. H. (2016). Low-frequency waves at comet 67p/Churyumov-Gerasimenko: Observations compared to numerical simulations. *Astronomy and Astrophysics*, 594, A66. <https://doi.org/10.1051/0004-6361/201628803>
- Li, T., Wang, Y., Chang, C., Hu, N., & Zheng, Y. (2014). Color-appearance-model based fusion of gray and pseudo-color images for medical applications. *Information Fusion*, 19, 103–114. <https://doi.org/10.1016/j.inffus.2012.07.002>
- Luo, M. R., & Hunt, R. W. G. (1998). *The structure of the CIE 1997 colour appearance model (CIECAM97s)* (Vol. 23). John Wiley & Sons.
- Mandt, K. E., Eriksson, A., Edberg, N. J. T., Koenders, C., Broiles, T., Fuselier, S. A., et al. (2016). RPC observation of the development and evolution of plasma interaction boundaries at 67p/Churyumov-Gerasimenko. *Monthly Notices of the Royal Astronomical Society*, 462(Suppl 1), S9–S22. <https://doi.org/10.1093/mnras/stw1736>
- Moroney, N., Fairchild, M., Hunt, R., Changjun, L., Luo, R. M., & Newman, T. (2002). The CIECAM02 color appearance model (Vol. 10, p. 23–27).
- Morse, D. L. (1976). A model for ion thermalization in the Earth's bow shock. *Journal of Geophysical Research*, 81(A34), 6126–6130. <https://doi.org/10.1029/JA081i034p06126>
- Neugebauer, M., Lazarus, A., Balsiger, H., Fuselier, S., Neubauer, F., & Rosenbauer, H. (1989). The velocity distributions of cometary protons picked up by the solar wind. *Journal of Geophysical Research: Space Physics*, 94(A5), 5227–5239. <https://doi.org/10.1029/JA094iA05p05227>
- Nilsson, H. (2021a). Rosetta-Orbiter 67P RPCICA 4 EXT2 Resampled and calibrated V1.0 [Dataset]. ESA Planetary Science Archive and NASA Planetary Data System. Retrieved from <https://pdssbn.astro.umd.edu/holdings/ro-c-rpica-4-ext2-phys-mass-v1.0/dataset.shtml>
- Nilsson, H. (2021b). Rosetta-Orbiter 67P RPCICA 5 EXT2 derived moment V1.0 [Dataset]. ESA Planetary Science Archive and NASA Planetary Data System. Retrieved from <https://pdssbn.astro.umd.edu/holdings/ro-c-rpica-5-ext2-moment-v1.0/dataset.shtml>
- Nilsson, H., Lundin, R., Lundin, K., Barabash, S., Borg, H., Norberg, O., et al. (2007). RPC-ICA: The ion composition analyzer of the Rosetta plasma consortium. *Space Science Reviews*, 128(1–4), 671–695. <https://doi.org/10.1007/s11214-006-9031-z>
- Nilsson, H., Wieser, G. S., Behar, E., Gunell, H., Wieser, M., Galand, M., et al. (2017). Evolution of the ion environment of comet 67p during the Rosetta mission as seen by RPC-ICA. *Monthly Notices of the Royal Astronomical Society*, 469(Suppl_2), S252–S261. <https://doi.org/10.1093/mnras/stx1491>

- Reinhard, R. (1987). The giotto mission to comet Halley. *Journal of Physics E: Scientific Instruments*, 20(6), 700–712. <https://doi.org/10.1088/0022-3735/20/6/029>
- Richter, I., Glassmeier, K.-H., Goetz, C., Koenders, C., Eichelberger, H., & Cupido, E. (2019). Rosetta-orbiter 67P RPCMAG 3 EXT2 calibrated V9.0 [Dataset]. ESA Planetary Science Archive and NASA Planetary Data System. Retrieved from <https://pdssbn.astro.umd.edu/holdings/ro-c-rpcmag-3-ext2-calibrated-v9.0/dataset.shtml>
- Skopke, N., Paschmann, G., Bame, S. J., Gosling, J. T., & Russell, C. T. (1983). Evolution of ion distributions across the nearly perpendicular bow shock: Specularly and non-specularly reflected-gyrating ions. *Journal of Geophysical Research*, 88(A8), 6121–6136. <https://doi.org/10.1029/JA088iA08p06121>
- Smith, N. J. (2015). Colorspacious [Software]. <https://doi.org/10.5281/zenodo.1214904>
- Taylor, M. G. G. T., Altobelli, N., Buratti, B. J., & Choukroun, M. (2017). The Rosetta mission orbiter science overview: The comet phase. *Philosophical Transactions of the Royal Society of London A: Mathematical, Physical and Engineering Sciences*, 375(2097). <https://doi.org/10.1098/rsta.2016.0262>
- Trantham, B. (2019). Rosetta-Orbiter 67P RPCIES 3 EXT2 V2.0 [Dataset]. ESA Planetary Science Archive and NASA Planetary Data System. Retrieved from <https://pdssbn.astro.umd.edu/holdings/ro-c-rpcies-3-ext2-v2.0/dataset.shtml>
- Williamson, H. N., Nilsson, H., Stenberg Wieser, G., Moeslinger, A., & Goetz, C. (2022). Development of a cometsheath at comet 67p/Churyumov-Gerasimenko. A case study comparison of Rosetta observations. *Astronomy and Astrophysics*, 660, A103. <https://doi.org/10.1051/0004-6361/202142461>
- Willmott, C. J. (1981). On the validation of models. *Physical Geography*, 2(2), 184–194. <https://doi.org/10.1080/02723646.1981.10642213>
- Wilson, L. B., III, Stevens, M. L., Kasper, J. C., Klein, K. G., Maruca, B. A., Bale, S. D., et al. (2018). The statistical properties of solar wind temperature parameters near 1 au. *The Astrophysical Journal - Supplement Series*, 236(2), 41. <https://doi.org/10.3847/1538-4365/aab71c>

References From the Supporting Information

- Clark, G., Broiles, T. W., Burch, J. L., Collinson, G. A., Cravens, T., Frahm, R. A., et al. (2015). Suprathermal electron environment of comet 67p/Churyumov-Gerasimenko: Observations from the rosetta ion and electron sensor. *Astronomy and Astrophysics*, 583, A24. <https://doi.org/10.1051/0004-6361/201526351>
- Nilsson, H., Moeslinger, A., Williamson, H. N., Bergman, S., Gunell, H., Wieser, G. S., et al. (2022). Upstream solar wind speed at comet 67p: Reconstruction method, model comparison, and results. *Astronomy and Astrophysics*, 659, A18. <https://doi.org/10.1051/0004-6361/202142867>